Ultramicroscopy 130 (2013) 70–76

Contents lists available at SciVerse ScienceDirect

Ultramicroscopy

journal homepage: www.elsevier.com/locate/ultramic

Quantitative spin polarization analysis in photoelectron emission microscopy with an imaging spin filter

Christian Tusche [a,*], Martin Ellguth [a], Alexander Krasyuk [a], Aimo Winkelmann [a], Dmytro Kutnyakhov [b], Pavel Lushchyk [b], Katerina Medjanik [b], Gerd Schönhense [b], Jürgen Kirschner [a,c]

[a] Max-Planck-Institut für Mikrostrukturphysik, 06120 Halle, Germany
[b] Institut für Physik, Johannes Gutenberg-Universitat Mainz, 55128 Mainz, Germany
[c] Naturwissenschaftliche Fakultät II, Martin-Luther-Universität Halle-Wittenberg, 06120 Halle, Germany

ARTICLE INFO

Available online 6 March 2013

Keywords:
Electron spin polarization analysis
Photoemission
Electron microscopy
Magnetic imaging

ABSTRACT

Using a photoelectron emission microscope (PEEM), we demonstrate spin-resolved electron spectroscopic imaging of ultrathin magnetic Co films grown on Cu(100). The spin-filter, based on the spin-dependent reflection of low energy electrons from a W(100) crystal, is attached to an aberration corrected electrostatic energy analyzer coupled to an electrostatic PEEM column. We present a method for the quantitative measurement of the electron spin polarization at 4×10^3 points of the PEEM image, simultaneously. This approach uses the subsequent acquisition of two images with different scattering energies of the electrons at the W(100) target to directly derive the spin polarization without the need of magnetization reversal of the sample.

1. Introduction

In the past decades, parallel imaging electron microscopy based on the cathode lens [1] has evolved into a powerful tool for the characterization and analysis of the unique properties of micro- and nano-structured systems. For instance, photoemission electron microscopy (PEEM) images the local distribution of electrons emitted from a sample surface upon the excitation by light. This is why, for instance, element-specific core level absorption of soft-X-rays can be used for element-resolved photoelectron emission microscopy, with the natural extension to magnetic nanostructure imaging using magnetic dichroism in the absorption of polarized radiation [2], and pico-second time resolution by stroboscopic excitation [3,4]. By applying sum rules in XMCD PEEM [5], the spin- and orbital-magnetic moment can be measured, quantitatively, on a local scale.

A slightly different approach is adopted in low energy electron microscopy (LEEM) [6], where the sample is illuminated by an electron beam of 1–100 eV in energy. Compared to emission microscopy, where the image forming electrons are emitted from the sample, the contrast in LEEM images is based on electrons diffracted at the sample surface. In the spin polarized variant, SP-LEEM [7], magnetic contrast is obtained by using a spin polarized primary electron beam, where an asymmetry in the diffracted intensities is mediated by exchange interaction at the ferromagnetic surface [8].

In principle, the most straightforward approach to the imaging of magnetic structures in PEEM is the analysis of the spin of electrons forming the image. Together with recent developments [9,10] which combine the photoemission microscope with the analysis of energy and momentum of the emitted photoelectrons, this approach enables the full characterization of all degrees of freedom of the photoelectrons on a local scale.

In electron spectroscopy, the analysis of the electron spin is typically accomplished by scattering at a target with a differing cross section for electrons with opposite spin projections on an axis determined by the details of the respective scattering setup. Typical configurations include the Mott detector using high energy scattering at a gold target, spin polarized low energy electron diffraction (SP-LEED), and low energy exchange scattering at a ferromagnetic target [11,12]. Such single channel detectors are, however, incompatible with parallel imaging electron microscopes. Therefore, in electron microscopy, the spin polarization of electrons emitted from the sample could only be measured in the scanning electron microscope with polarization analysis (SEMPA), where the polarization vector of secondary electrons is analyzed while the focused electron beam is scanned over the sample [13].

Only recently, more efficient multi-channel spin filters became available, based on specular reflection of electrons in the (00)-LEED beam at a single crystal surface. Like in LEEM, the reflection of electrons at a crystalline surface can, in principle, transfer a

* Corresponding author. Tel.: +49 3455582698; fax: +49 3455511223.
E-mail address: tusche@mpi-halle.mpg.de (C. Tusche).

0304-3991/$ - see front matter © 2013 Elsevier B.V. All rights reserved.
http://dx.doi.org/10.1016/j.ultramic.2013.02.022

high resolution electron optical image. It has been demonstrated that, by placing such an electron mirror in the electron beam path of a PEEM, spin resolved PEEM images of the magnetic domain structure of the surface are obtained with a resolution of 300 nm in the simultaneously acquired image [14]. The intensity contrast between electrons of different spin is obtained due to spin–orbit coupling in the high-Z material of the target, in this case W(100) [15]. Moreover, the same approach can be combined with classical hemispherical electron spectrometers, where the two-dimensional distribution of kinetic energy and emission angles in the exit field of the analyzer is spin filtered simultaneously [16]. We report on the spin resolved spectroscopic imaging using this mirror type imaging spin filter, installed in an energy filtered photoelectron emission microscope. In addition to the intensity contrast between magnetic domains, a method is presented to measure the sign and magnitude of the spin polarization at every image point.

2. Experimental setup

The experimental setup is outlined in Fig. 1. The spin-filter is installed in our "momentum microscope". This instrument, based on a commercial design (Omicron NanoESCA) [9], combines a PEEM column with an aberration corrected electrostatic energy analyzer, consisting of two hemispherical energy analyzers. Energy selection is accomplished by the first (bottom) hemispherical analyzer, while the aberrations introduced at this stage are canceled out by reversing the beam path in the second anti-symmetrical analyzer. When the microscope is operated as an energy filtered PEEM, the spatial image of the sample is obtained at the exit of the energy analyzer with an energy resolution of about 200 meV and a magnification factor up to 140. A detailed description of this instrument is published elsewhere [10]. The spin-filter is inserted into the electron optical path right after the energy analyzer. At this point, the electron kinetic energy is equal to the pass energy of the analyzer, set to $E_{Pass} = 100$ eV. An electrostatic retarding lens decelerates the electrons from the pass energy to the scattering energy, E_{Scatt}. Under practical conditions, scattering energies in the range of 15–90 eV can be used.

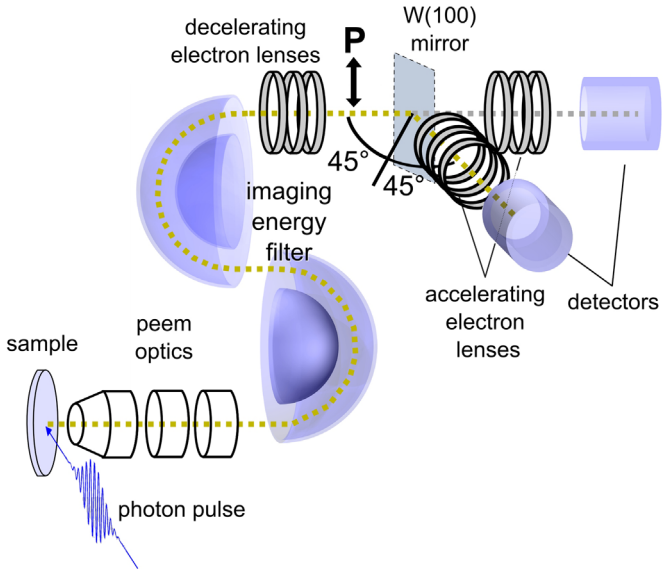

Fig. 1. Experimental setup of the imaging spin filter installed at the energy filtered photoelectron emission microscope, consisting of the sample illuminated by laser light, the PEEM optics, and the imaging energy filter. Electrons are decelerated and accelerated by electrostatic lenses before and after scattering at the W(100) mirror. Images are collected at the detectors in straight and mirrored geometry. The quantization axis, *P*, is normal to the scattering plane.

A reciprocal image is formed at the W(100) scattering target, such that the spatial image information is encoded by small deviations in the angle of incidence around the ideal value of 45°. This image information is conserved upon the mirror like specular reflection in the achromatic (00)-LEED beam. Electrons then are accelerated again by an electrostatic lens, and the spin filtered image is formed on the detector in the 90° mirrored geometry, where the quantization axis (*P*) is oriented normally to the scattering plane. When the crystal is retracted from the beam path, the spin-integrated image is obtained on the detector in the straight-line geometry.

Energy filtered PEEM images were recorded using two-photon photoemission (2PPE). We use 3.1 eV *p*-polarized photons from the second harmonic of a pulsed Ti:Sa laser system with a pulse length of 20 fs and a repetition rate of 80 MHz. The laser spot on the sample is focused to a size of about 20 μm. In order to obtain an uniform illumination of the field-of-view, the laser focus was periodically scanned over the imaged area with a frequency of about 10 times per second. The Cu(100) single crystal was cleaned by cycles of argon ion sputtering and annealing until sharp electron diffraction patterns were obtained and no traces of contamination were visible in Auger electron spectroscopy. The crystal quality was further checked by momentum resolved photoemission, using He-I radiation from a discharge lamp [17]. The cobalt films with a thickness of 8.0 ± 0.3 monolayers (ML), calibrated by medium energy electron diffraction, were grown by thermal evaporation from a high purity Co rod onto the clean Cu(100) crystal, at a temperature of 400 K.

Before the spin resolved measurements, the W(100) electron mirror was prepared by several cycles of flashing (1700 K) in 5×10^{-8} mbar O_2 atmosphere, and a final high temperature (2500 K) flash removing the oxide layer. This well established procedure is known to lead to clean, carbon free surfaces of W(100) [18].

3. Magnetic imaging

Fig. 2 shows a series of PEEM images of the magnetic domain structure of the as-grown cobalt film recorded in the 90° reflected imaging column. The magnetization direction in the black and white domain in the image is aligned along the vertical direction as indicated in Fig. 2a, parallel to the quantization axis of the spin filter. This was checked by azimuthal rotation of the sample, in order to obtain the maximum contrast. Here, the magnetization direction is found along the [001] direction. The spin filter always measures the projection of the polarization vector onto the vertical quantization axis (see Fig. 1). Thus, for an azimuthal rotation by 90°, the magnetic contrast between the domains in Fig. 2 disappears.

For Fig. 2a–c, the initial state energy of the photoelectrons was fixed at 0.3 eV below the Fermi level. In 2PPE, the spin polarization of photoelectrons at this energy was reported to be in the order of 40–50%, for films of comparable thickness [19,20]. The scattering energy is varied from 23 eV (Fig. 2a) to 31 eV (Fig. 2c) by changing the electrode voltages of the decelerating and accelerating lens, such that the image focusing and magnification stay constant. For all scattering energies, the exposure time is 60 s.

In Fig. 2a, the scattering energy was set to 23 eV. At this energy, a weak contrast between a bright and a dark magnetic domain is observed. The image shows the intensity information recorded on the CCD camera on a linear scale (see the gray bar in the figure). The raw CCD image data were divided by a background image (flat field), to correct for inhomogeneities of the detector and spatial variation in the reflectivity of the W(100) mirror.

When the scattering energy is changed to $E_{Scatt} = 27$ eV (Fig. 2b) the contrast between both domains is strongly increased. This scattering energy is at the optimum working point for highest spin sensitivity, as reported earlier [14]. The measurement of a spin filtered intensity image at this working point provides an efficient way for quantitative measurement of the size and shape of domains on a magnetic sample. The relative change in magnetization then is given by the intensities in the respective domains. By further increasing the scattering energy to 31 eV as shown in Fig. 2c, contrast decreases. While the contrast and the intensity of the image changes as function of the scattering energy, the imaged area and magnification are the same for all energies. This, in principle, allows using images taken at different scattering energies to compute quantities like the absolute spin polarization, as we will show below.

The detailed variation of the spin sensitivity and reflectivity of the W(100) electron mirror around the working point of $E_{Scatt} = 27$ eV was studied by recording images in steps of $\Delta E_{Scatt} = 0.5$ eV. The intensity of the bright and dark domain was evaluated by integration over rectangular areas located close to the center of the image, as indicated in Fig. 2a. This corresponds to an angle of incidence of the electrons at the W(100) crystal of about 45°.

4. Spin polarization measurement

Fig. 3a shows the spin averaged reflectivity for 45° angle of incidence. Here, the absolute value of the reflectivity was obtained by the ratio of the single-electron count rates measured on the multi-channel plate detectors in the spin-filtered and non-spin-filtered detector branches. In the measured scattering energy range, we find a maximum reflectivity of 1.35% at $E_{Scatt} = 25$ eV, i.e. close to the 27 eV image shown in Fig. 2b, above, and a second local maximum of 1.30% at $E_{Scatt} = 30.5$ eV. Further increasing the scattering energy leads to a reduction of the reflectivity to a value of 0.30% at $E_{Scatt} = 40$ eV, i.e. by a factor of ≈ 5. Measurements in a wider energy range up to $E_{Scatt} = 90$ eV [14] show that the reflectivity is further reduced towards higher scattering energies by two orders of magnitude compared to the maximum at 25.5 eV. For the application as imaging spin filter it is therefore preferable to use a working point at a low scattering energy, where the reflectivity is high.

In order to compare the efficiency of the imaging spin filter to state-of-the-art single channel detectors, the 2D detection efficiency, $\mathcal{F}_{2D}$, was introduced [14,16]

$$\mathcal{F}_{2D} = S^2 \frac{I}{I_0} \cdot N \tag{1}$$

Here, S accounts for the spin sensitivity, i.e. the measured asymmetry of reflected intensities for an electron beam with a 100% spin polarization. In dependence on the scattering energy at the W(100) crystal, the sign of S takes into account that positive or negative, as well as zero asymmetries can be measured for a constant non-zero spin polarization of the electron beam. The spin-averaged reflectivity is I/I_0 and the simultaneous acquisition of all image points is accounted for by the number of resolvable image points N.

Fig. 3b shows the variation of the spin sensitivity as a function of the scattering energy measured in the same energy range as above. The spin sensitivity S corresponds to the intensity asymmetry that would be observed for a beam of fully polarized electrons. It is related to the measured asymmetry, A, in the two domains by $A = S \cdot P$, where P is the electron spin polarization. While previous measurements [14] showed a strong variation of the asymmetry in the energy range from 15 eV to 90 eV, Fig. 3b details the energy range from 20 eV to 40 eV, i.e. close to the working point of the spin filter. A clear maximum of the spin sensitivity, S, is located at the scattering energy $E_{Scatt} = 26.5$ eV, with a value of $S = 0.42$. For comparison, the spin filtered PEEM image in Fig. 2b was recorded at $E_{Scatt} = 27$ eV, very close to this best scattering energy. Remarkably, by changing the scattering energy by only 4 eV, we find a pronounced reduction of S to a value of 0.06 (compare also Fig. 2c). The scattering energy also coincides with the maximum reflectivity in Fig. 3a. As Eq. (1) contains an S^2 term, $E_{Scatt} = 30.5$ eV would lead to a strongly reduced 2D detection efficiency, compared to $E_{Scatt} = 26.5$ eV.

However, the strong variation of S within a small energy interval can be exploited to measure the lateral distribution of the absolute value of the spin polarization, $P(x,y)$, of photoelectrons emitted from the sample. The spin polarization is evaluated at each coordinate (x,y) of the spin filtered image. In the case of a real space PEEM image, this corresponds to the spatial coordinate on the sample. As was shown before, a lateral resolution of 300 nm can be obtained in the spin filtered PEEM image [14]. For the measurement of $P(x,y)$, the same image is acquired at the scattering energies $E_{Scatt} = 26.5$ eV and $E_{Scatt} = 30.5$ eV with maximum and minimum spin sensitivity, respectively. The spin polarization at each image point then is formally given as (see the Appendix for the derivation)

$$P(x,y) = \frac{1 - \varrho(x,y) \cdot \psi(x,y)}{\varrho(x,y) \cdot \psi(x,y) \cdot S_l(x,y) - S_h(x,y)} \tag{2}$$

Here, we define $\psi(x,y) = I_h(x,y)/I_l(x,y)$ as the ratio of the intensities $I_h(x,y)$ and $I_l(x,y)$ at each image point, measured using the scattering energy with high (h) or low (l) spin sensitivity, respectively. In the same way, the variation in reflectivity is accounted for by $\varrho = R_l(x,y)/R_h(x,y)$, the ratio of the spin integrated reflectivity $R_l(x,y)$ and $R_h(x,y)$, at both scattering energies.

We note that for the special case, where the spin sensitivity $S = S_h = -S_l$ is exactly reversed between the (h) and (l) measurements, and equal reflectivity, $R_h = R_l$, Eq. (2) can be simplified to

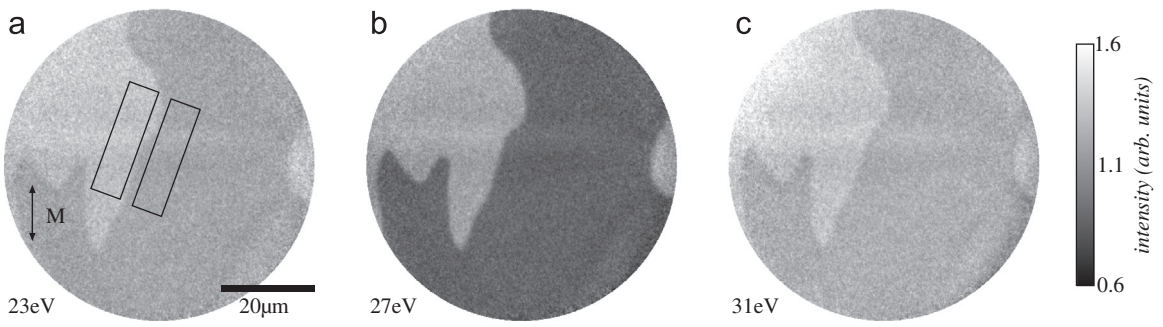

Fig. 2. PEEM images of the magnetic domain structure of the 8 ML cobalt film recorded after reflection at the W(100) crystal at a scattering energy of (a) $E_{Scatt} = 23$ eV, (b) $E_{Scatt} = 27$ eV and (c) 31 eV. All images show the same 60 μm field-of-view and were recorded at 300 meV below the Fermi level. The absolute intensity gray scale is the same for all images.

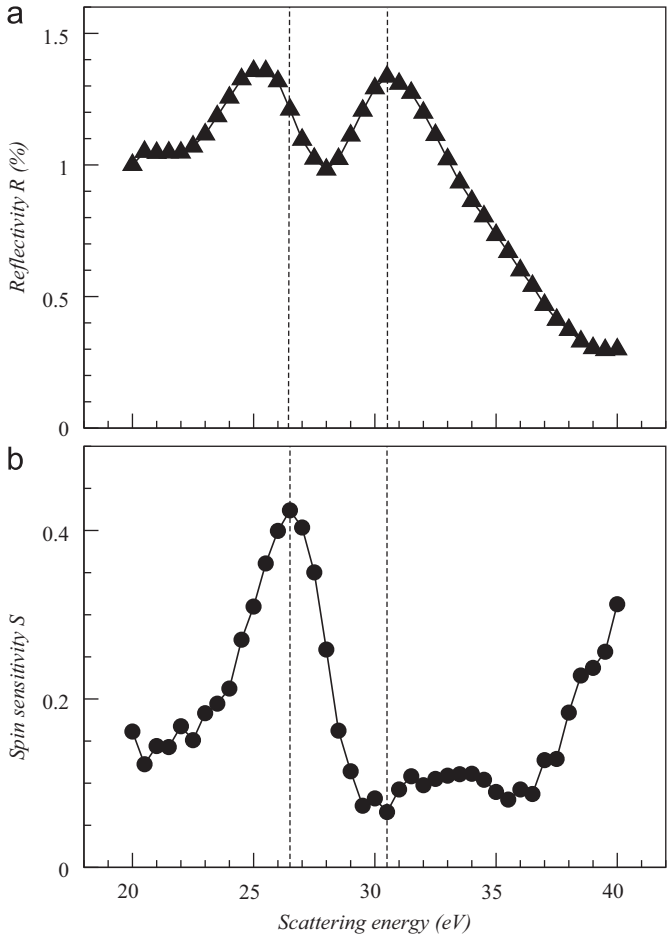

Fig. 3. (a) Spin integrated reflectivity, R, of the W(100) mirror as a function of scattering energy, measured by the ratio of the intensity in the 90° reflected image to the intensity in the direct image. (b) Spin sensitivity, S, as a function of scattering energy. The dashed lines at $E_{Scatt}=26.5$ eV and=30.5 eV mark the working points with a spin sensitivity of S=0.42 and S=0.06, respectively.

the well known asymmetry expression where the spin polarization is given by

$$P(x,y)=\frac{1}{S}\cdot\frac{I_h(x,y)-I_l(x,y)}{I_h(x,y)+I_l(x,y)} \tag{3}$$

This situation would, for instance, apply when two measurements were taken at the fixed 26.5 eV scattering energy working point, reversing the magnetization of the sample between the (h) and (l) images.

In the general form of Eq. (2), the spin integrated reflectivity ratio $\varrho(x,y)$ and the spin sensitivities $S_h(x,y)$ and $S_l(x,y)$ depend on the coordinate (x,y) in the image. This can be easily understood as the angle of incidence varies over the image. The value of the reflectivity and spin sensitivity presented in Fig. 3 were measured in the center of the image, i.e. with the angle of incidence equal to 45°. Electron optical simulations show that the angle of incidence ranges from 46.5° to 43.5° from the left to the right edge of the image, respectively.

Fig. 4a shows the variation of the spin integrated reflectivity ratio, $\varrho(x,y)$, over the area of the screen (18 mm diameter). The image was obtained experimentally by measuring unstructured PEEM images of the clean Cu(100) surface, illuminated by a mercury discharge lamp. Images were acquired at the scattering energies 30.5 and 26.5 eV. The ratio of the reflected intensities shows a monotonous variation over the complete image, whereas an average value of ≈ 1 is observed. A more quantitative picture is given in Fig. 4b by the line profile plotted along the diameter of Fig. 4a. As indicated in the figure, the horizontal position in the image circle can be related to the angle of incidence, α_i, defined as the angle of the incoming electron with respect to the surface normal of the W(100) crystal. In the range of $\alpha_i=45\pm1.5°$, the ratio of the reflectivity can be approximated by a linear behavior, both, in the x- and y-coordinates.

This linear dependence on the horizontal scattering angle can be easily understood as only a small $\pm1.5°$ variation of the angle is involved. In particular, as displayed in Fig. 3a, the working point at 26.5 eV is not directly located in the reflectivity maximum, but at the slope towards higher energy. At such points, a variation of the scattering conditions, either by a variation of the scattering energy, or the angle is expected to result in a changed reflectivity [16]. By the same argument, little variation is expected for the spin sensitivity around the local maximum and minimum at 26.5 eV and 30.5 eV, respectively. For a detailed quantitative understanding, however, it has to be noted that the observed maxima and minima in the reflectivity result from multiple scattering. Likewise, because of spin–orbit coupling, electrons with opposite spin see different potentials, leading to different scattering amplitudes and the observed asymmetry function [21].

In order to test this model, we derive the spatial distribution of spin polarization in the magnetic domains of an 8 ML thick cobalt film. Therefore, two spin filtered PEEM images were recorded in 2PPE with the analyzer set to a kinetic energy 0.8 eV below the Fermi edge. Fig. 5a and b shows the images acquired at $E_{Scatt}=26.5$ eV and 30.5 eV, respectively, with an integration time of 300 s, each. As already observed in Fig. 2, we find a changed contrast between the black and white domain, respectively. For the quantitative evaluation according to Eq. (2), we use the measured spin integrated reflectivity data, $\varrho(x,y)$, presented in Fig. 4. For the spin sensitivity, S, we assume a sufficiently small variation over the field-of-view, and use a constant value $S_h(x,y)=S_{26.5\ eV}$ or $S_l(x,y)=S_{30.5\ eV}$ for each scattering energy, and the simplified expression as

$$P(x,y)=\frac{1-\varrho(x,y)\cdot\psi(x,y)}{\varrho(x,y)\cdot\psi(x,y)\cdot S_{30.5\ eV}-S_{26.5\ eV}} \tag{4}$$

The result is displayed in Fig. 5c on a blue-to-red color scale (see the color bar in the figure). Here, the magnetic domains, visible in Fig. 5a by the intensity contrast, show an average spin polarization of $+0.40\pm0.05$ (red) and -0.40 ± 0.05 (blue). In principle, the information on the geometry of the magnetic domains is already accessible from the intensity image, e.g. it was demonstrated before that the width of the domain wall of the cobalt film can be extracted from the intensity image [14]. However, the intensity contrast does not directly contain the information about the relative orientation of magnetization, and is superimposed by other origins of contrast in the PEEM image. For instance, Fig. 5a shows a number of defects, labeled A, B and C, on the left side of the image, which show up as dark areas. The magnetic information is provided by the spin polarization image. Fig. 5c reveals that the structures labeled A and C have indeed positive spin polarization. By contrast, the structure labeled B is actually a small magnetic domain with a measured spin polarization of -0.15 ± 0.05, which could result from a rotated magnetization direction or a reduced spin polarization due to defects.

Fig. 5d shows a profile of the spin polarization across the domain boundary Fig. 5c. The profile reveals a sharp step in the polarization from the positive to the negative value. The width of this step is basically limited by the number of resolvable image points in the polarization image. Using a Gaussian line profile, the width of the step is in the order of 7 pixels on the CCD camera, while the diameter of the image is 460 pixels. This corresponds to 66 discrete points measured along a line over the diameter of the

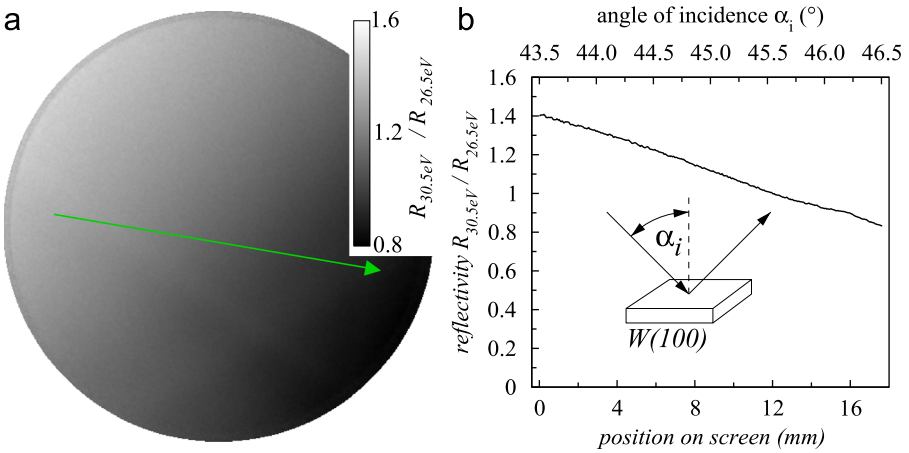

Fig. 4. (a) Map of the ratio of the spin integrated reflectivity, measured at $E_{Scatt} = 30.5$ eV and 26.5 eV, using unpolarized electrons from the clean Cu(100) surface. (b) Plot of the reflectivity ratio along the line in (a) as a function of the position on the screen (lower scale) or as a function of the angle of incidence, α_i, (upper scale).

image. The circular area of the spin polarization image thus contains a total number of about 3.5×10^3 points. This number is directly related to the gain in measurement efficiency compared to single-channel detectors due to the simultaneous detection of 3.5×10^3 statistically independent data points. We note that for obtaining improved statistics of the spin polarization in one uniform magnetic domain, independent data points could be averaged in the selected region. The observed image resolution is in good agreement with the resolution reported before for intensity images [14]. Electron optical simulations show that the number of resolvable spin channels is not limited by the resolution of the electron optics. As the image information is encoded in the angle of incidence, the fundamental limitation for the number of resolvable points is the angular broadening of the electron beam after diffraction at the spin filter target. For a high image resolution it is therefore required to use a high quality single crystal with a small mosaic spread. For the W(100) crystal we used in these experiments, the number of resolvable points in the interval of scattering angles of $\pm 1.5^\circ$ corresponds to an angular resolution of 0.05°. While this represents a good number for a W(100) single crystal, recent developments suggest that tungsten crystals with a significantly smaller mosaic spread might become available [22].

Fig. 5e shows a spin polarization image of a second sample with a cobalt thickness of 12 ML. Here, measured at a kinetic energy of 0.3 eV below the Fermi edge, we again find a spin polarization of ± 0.40 in the red and blue domain, respectively. The spin polarization does not significantly change between the 8 and 12 ML films. This can be understood, as the observed large spin polarization value of 0.4 results mainly from resonant transitions involving unoccupied states in the cobalt film [20]. The 2PPE experiment therefore selectively probes the electronic structure of the cobalt film, and a thickness dependent contribution of unpolarized electrons from the copper substrate is not dominant.

For the calculation of the spin polarization, we used a constant spin sensitivity $S_{26.5\ eV}$ and $S_{30.5\ eV}$ which do not depend on the image coordinate, i.e. on the angle of incidence of the LEED reflection at the W(100) crystal. By contrast, the relative spin integrated reflectivity, ϱ, exhibits a gradient from the left to the right side of the image, included in the analysis. The variation of spin polarization from the left to the right side of the image, along the drawn line, is plotted in Fig. 5f. Here, we do not find a systematic variation of the measured spin polarization as a function of the scattering angle. This result indicates that the variation of the scattering geometry over the field-of-view results mainly in a variation of the spin integrated reflectivity, that can be accounted for experimentally by the measurement of a reference image at each energy.

5. Summary

We have demonstrated spin resolved spectroscopic imaging by combining a spin polarizing electron mirror with an energy filtered electrostatic photoelectron emission microscope. The procedure for the quantitative measurement of the spin polarization in the PEEM image exploits the scattering energy dependence inherent to the spin polarized LEED process at the W(100) crystal. We use two working points in the scattering energy landscape at $E_{Scatt} = 26.5$ eV and 30.5 eV, where the spin sensitivity is $S_{26.5\ eV} = 0.42$ and $S_{30.5\ eV} = 0.06$, respectively. Changing the scattering energy only requires to change few electrode voltages in the electron optical system, such that a fast and reproducible switching between both working points is possible. From the images recorded at both scattering energies, the spin polarization image is calculated using the expression in Eq. (4).

As the spin sensitivity is sufficiently constant over the image, only a constant value for $S_{26.5\ eV}$ and $S_{30.5\ eV}$ at each working point is required. The additional calibration parameter ϱ, i.e. the spin integrated reflectivity ratio, can be directly measured experimentally by acquiring reference images of a non-polarized surface, e.g. the clean Cu(100) substrate, in defocussed condition.

The general expression of Eq. (2) does not require the restriction of constant spin sensitivity. Therefore, Eq. (2) also allows to calculate the electron spin polarization when the imaging spin filter is used behind a dispersive hemispherical energy analyzer, where either the x or y image coordinate correlates with the scattering energy [16]. Operating the analyzer in a way that the simultaneously acquired energy window is scanned over the measured spectrum, each kinetic energy point can be acquired once at each scattering energy within an interval between 26.5 and 30.5 eV. According to Eq. (2) the spin polarization then can be calculated from any two of these points with equal measured kinetic energy but different scattering energies. It was shown recently that the required values for the reflectivity and spin sensitivity as a function of the scattering-energy and scattering-angle can be derived by spin polarized LEED calculations within the layer-Korringa–Kohn–Rostoker (KKR) framework, and verified experimentally [23].

We are currently investigating materials other than W(100) to be used as the spin filtering electron mirror. In particular, a high

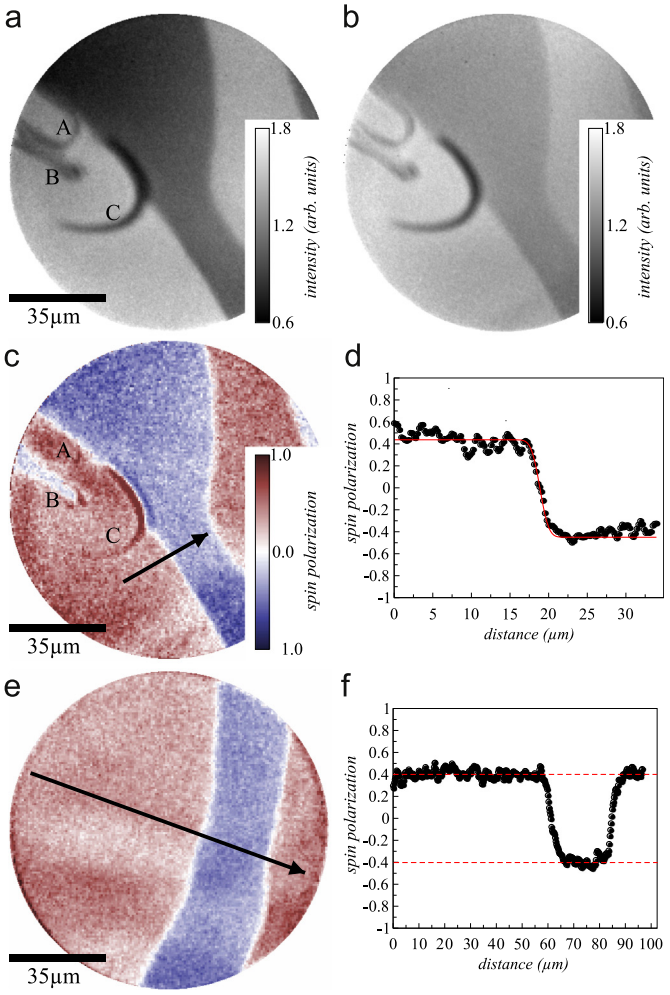

Fig. 5. (a) Spin filtered PEEM image of a 8 ML Co film measured at $E_{Scatt} = 26.5$ eV. (b) The same image measured at $E_{Scatt} = 30.5$ eV. (c) Calculated spin polarization image from (a) and (b), the color code is indicated by the bar. (d) Spin polarization (symbols) plotted along the line in (c), and a fit (solid line) assuming a Gaussian broadening. (e) Spin resolved PEEM image of a 12 ML Co film. (f) Profile along the line in (e). Horizontal dashed lines at $P=0.4$ and $P=-0.4$ serve as a guide to the eye.

crystalline quality of the scattering target is necessary, such that the number of resolvable image points can be increased. This would directly lead to an improvement in the 2D detection efficiency. Spin-filtering is not limited to spatial PEEM images. The presented results are a prerequisite for the quantitative measurement of the photoelectron spin polarization in momentum microscopy. The latter allows one to record the momentum distribution of photoelectrons using the same instrument, while spin polarized information can be obtained in the same way as demonstrated for spatial images.

Acknowledgments

We would like to thank M. Escher and N. Weber from Focus GmbH for the electron optical design and construction of the 2D spin filter.

Appendix A

Here, we derive the spin polarization from scattered intensity values using two distinct scattering energies. The differential cross section σ for elastic scattering of a polarized beam of electrons can be written as [24]

$$\sigma(\theta,\phi) = R(\theta)(1+S(\theta)\vec{P}\cdot\hat{n}) \tag{5}$$

where θ and ϕ are the polar and azimuthal angles, respectively, $\hat{n}$ is the scattering plane normal, $R(\theta)$ is the spin integrated scattering amplitude and $S(\theta)$ is the spin sensitivity, also termed Sherman function. From Eq. (5) it is evident that, in a kinematic model, the scattering cross section only depends on the polar scattering angle. By contrast, for scattering at a solid surface, dynamical theory and experiment [15,21] show that R and S depend on the polar and azimuthal angles, due to multiple scattering. As the spatial coordinate (x,y) in the spin filtered image is encoded in variations of the angles θ and ϕ, we write $R=R(x,y)$ and $S=S(x,y)$.

Only the component of the polarization vector $\vec{P}$ parallel to the scattering plane normal $\hat{n}$ can be measured. Therefore, we discard the other components and use the abbreviation $P=\vec{P}\cdot\hat{n}$. The scattering cross section is proportional to the ratio of the scattered electron photo current I_1 to incident photo current I_0. When using two different scattering energies labeled by the indices h and l, we obtain scattered intensities I_h, I_l for each case

$$I_h = I_0(x,y)(1+S_h(x,y)P(x,y))R_h(x,y) \tag{6}$$

$$I_l = I_0(x,y)(1+S_l(x,y)P(x,y))R_l(x,y) \tag{7}$$

Dividing Eq. (6) by (7), we obtain

$$\rho(x,y)\psi(x,y) = \frac{1+S_h(x,y)P(x,y)}{1+S_l(x,y)P(x,y)}, \tag{8}$$

where $\rho = R_l/R_h$ and $\psi = I_h/I_l$. Solving for P, we arrive at

$$P(x,y) = \frac{1-\rho(x,y)\psi(x,y)}{\rho(x,y)\psi(x,y)S_l(x,y)-S_h(x,y)} \tag{9}$$

References

[1] E. Bauer, Journal of Physics: Condensed Matter 21 (2009) 314001.
[2] C.M. Schneider, G. Schönhense, Reports on Progress in Physics 65 (2002) 1785–1839.
[3] J. Vogel, W. Kuch, M. Bonfim, J. Camarero, Y. Pennec, F. Offi, K. Fukumoto, J. Kirschner, A. Fontaine, S. Pizzini, Applied Physics Letters 82 (2003) 2299–2301.
[4] A. Krasyuk, A. Oelsner, S. Nepijko, A. Kuksov, C. Schneider, G. Schönhense, Applied Physics A 76 (2003) 863–868.
[5] W. Kuch, J. Gilles, S.S. Kang, S. Imada, S. Suga, J. Kirschner, Physical Review B 62 (2000) 3824–3833.
[6] E. Bauer, Reports on Progress in Physics 57 (1994) 895.
[7] N. Rougemaille, A.K. Schmid, European Physical Journal—Applied Physics 50 (2010) 20101.
[8] R. Feder, Physical Review B 15 (1977) 1751–1754.
[9] M. Escher, N. Weber, M. Merkel, C. Ziethen, P. Bernhard, G. Schönhense, S. Schmidt, F. Forster, F. Reinert, B. Krömker, D. Funnemann, Journal of Physics: Condensed Matter 17 (2005) S1329–S1338.
[10] B. Krömker, M. Escher, D. Funnemann, D. Hartung, H. Engelhard, J. Kirschner, Review of Scientific Instruments 79 (2008) 053702.
[11] D. Yu, C. Math, M. Meier, M. Escher, G. Rangelov, M. Donath, Surface Science 601 (2007) 5803–5808.
[12] A. Winkelmann, D. Hartung, H. Engelhard, C.-T. Chiang, J. Kirschner, Review of Scientific Instruments 79 (2008) 083303.
[13] H. Oepen, M. Benning, H. Ibach, C. Schneider, J. Kirschner, Journal of Magnetism and Magnetic Materials 86 (1990) L137–L142.
[14] C. Tusche, M. Ellguth, A.A. Ünal, C.-T. Chiang, A. Winkelmann, A. Krasyuk, M. Hahn, G. Schönhense, J. Kirschner, Applied Physics Letters 99 (2011) 032505.
[15] J. Kirschner, R. Feder, Physical Review Letters 42 (1979) 1008–1011.
[16] M. Kolbe, P. Lushchyk, B. Petereit, H.J. Elmers, G. Schönhense, A. Oelsner, C. Tusche, J. Kirschner, Physical Review Letters 107 (2011) 207601.
[17] A. Winkelmann, C. Tusche, A.A. Ünal, M. Ellguth, J. Henk, J. Kirschner, New Journal of Physics 14 (2012) 043009.
[18] K. Zakeri, T. Peixoto, Y. Zhang, J. Prokop, J. Kirschner, Surface Science 604 (2010) L1.
[19] O. Andreyev, Y.M. Koroteev, M.S. Albaneda, M. Cinchetti, G. Bihlmayer, E.V. Chulkov, J. Lange, F. Steeb, M. Bauer, P.M. Echenique, S. Blügel, M. Aeschlimann, Physical Review B 74 (2006) 195416.

[20] C.-T. Chiang, A. Winkelmann, J. Henk, F. Bisio, J. Kirschner, Physical Review B 85 (2012) 165137.
[21] R. Feder, Journal of Physics C: Solid State Physics 14 (1981) 2049.
[22] S. Bozhko, V. Glebovsky, V. Semenov, I. Smirnova, Journal of Crystal Growth 311 (2008) 1.
[23] D. Kutnyakhov, P. Lushchyk, A. Fognini, D. Perriard, M. Kolbe, K. Medjanik, E. Fedchenko, S. Nepijko, H. Elmers, G. Salvatella, C. Stieger, R. Gort, T. Bähler, T. Michlmayer, Y. Acremann, A. Vaterlaus, F. Giebels, H. Gollisch, R. Feder, C. Tusche, A. Krasyuk, J. Kirschner, G. Schönhense, Ultramicroscopy, this issue.
[24] J. Kessler, Polarized Electrons, 2nd edition, Springer-Verlag, Berlin, Heidelberg, New York, Tokyo, 1985, ISBN: 0-387-15736-0.